Large-Scale Surface Air Temperature Bias in Summer over the CONUS and Its Relationship to Tropical Central Pacific Convection in the UFS Prototype 8

NAKBIN CHOI[a] AND CRISTIANA STAN[a]

[a] *Department of Atmospheric, Oceanic and Earth Sciences, George Mason University, Fairfax, Virginia*

(Manuscript received 2 February 2024, in final form 12 September 2024, accepted 20 October 2024)

ABSTRACT: This study aims to understand the source of surface air temperature bias over the contiguous United States (CONUS) during boreal summer (June–September) in the Unified Forecast System (UFS) coupled model prototype 8 (P8), developed by the National Centers for Environmental Prediction (NCEP) and the National Oceanic and Atmospheric Administration (NOAA). The focus is on the subseasonal variability defined as a weekly average in weeks 2–5 of forecast leads (total 224 cases; 4 weeks × 2 initialization dates × 4 months × 7 years). The large-scale surface air temperature bias pattern is extracted using the empirical orthogonal function (EOF) analysis. The associated principal component describes the variability of bias for each reforecasting week throughout the 2011–17 reforecasting period. The leading EOF of surface air temperature bias exhibits an east–west dipole pattern over the CONUS, explaining 31.6% of the total variability of weekly temperature bias. This bias pattern is strongly related to the upper-level Rossby wave induced by a bias in convection over the central tropical Pacific. Furthermore, the mean bias of background flow in the extratropics degrades the representation of teleconnections from the tropics to the midlatitudes. UFS P8 has weaker zonal wind over the North Pacific with stronger vertical wind shear than the ERA5 reanalysis. The weak zonal wind hampers the Rossby wave's propagation, while strong vertical shear reduces its amplitude.

KEYWORDS: Atmospheric circulation; Teleconnections; Model errors; Model evaluation/performance; Numerical weather prediction/forecasting

1. Introduction

The most extreme weather events, such as tropical cyclones, heatwaves, and cold surges, occur on subseasonal time scales between a week to a month (Vitart and Robertson 2018; Vitart et al. 2019; Robertson et al. 2020; Domeisen et al. 2022). The high impact of these events on societal activities and human health underscores the importance of subseasonal to seasonal forecasting (White et al. 2017; Merz et al. 2020; White et al. 2022). The forecast skill on subseasonal to seasonal (S2S) time scales is affected by all Earth system components: atmosphere, land, ocean, and sea ice (Meehl 1995; Koster et al. 2010; Orsolini et al. 2013; Robertson et al. 2015; Guemas et al. 2016). That means using a fully coupled climate model is necessary for the skillful prediction of S2S time scales.

Despite the existence of numerous state-of-the-art coupled models for S2S forecasting (NCEP; Saha et al. 2006; GFDL; Delworth et al. 2020; NASA; Molod et al. 2020; ECMWF; Vitart 2014; UKMO; Williams et al. 2018), subseasonal prediction is still a challenging field. The sources of predictability in the S2S time scale come from various factors such as atmosphere–ocean/atmosphere–land interactions (Peng and Kumar 2005; Saravanan and Chang 2019; Dirmeyer et al. 2019; Seo et al. 2024), tropics to midlatitudes teleconnections (Stan et al. 2017; Lin et al. 2019), and stratosphere–troposphere coupling (Domeisen et al. 2020; Stan et al. 2022).

The National Centers for Environmental Prediction (NCEP) of the National Oceanic and Atmospheric Administration (NOAA) developed a new S2S l forecast system, the Unified Forecast System (UFS), as a community Earth modeling system. The initial development phase of UFS was carried out across eight prototypes. A detailed comparison of the first seven prototypes is given in Stefanova et al. (2022). The UFS combines model components for the atmosphere, land, ocean, sea ice, and waves. The last prototype has an additional aerosol component.

While UFS is a global model, one of the target areas for forecasting is the contiguous United States (CONUS). The weather and climate of the CONUS is affected by teleconnections induced by tropical Pacific variability such as the Madden–Julian oscillation (MJO) and El Niño–Southern Oscillation (ENSO) (Jenney et al. 2019; Jong et al. 2021; Stan et al. 2022; Park et al. 2023; Williams et al. 2023). Krishnamurthy et al. (2021) examined the subseasonal predictability of the UFS prototype 2 during boreal summer and found reasonable skill for low-level horizontal wind and 2-m temperature, especially over the western CONUS. The source of predictability was attributed to ENSO and an intraseasonal oscillation (ISO) from the Pacific. The prediction of precipitation is less skillful. Krishnamurthy and Stan (2022) evaluated the predictability of extreme precipitation and temperature over CONUS in the UFS prototype 5. They have shown that the predictability of these events is also affected by the ENSO and Pacific ISO. Interestingly, the model does not predict the extreme values of minimum and maximum temperature over large western regions of

Supplemental information related to this paper is available at the Journals Online website: https://doi.org/10.1175/JCLI-D-24-0078.s1.

Corresponding author: Nakbin Choi, nchoi21@gmu.edu

DOI: 10.1175/JCLI-D-24-0078.1

CONUS. The number of extreme precipitation events is overestimated, and the location and amplitude of events have large errors.

Because the prediction of tropical variability is affected by biases, they can also induce forecast biases over the CONUS. Stan et al. (2023) and Bai et al. (2023) investigated the impact of tropical SST bias on the forecast biases over the CONUS in the UFS prototypes 5 and 6, respectively. Both studies found robust mean biases in surface air temperature and precipitation during weeks 1–4 of the forecast. However, the bias patterns vary from week to week. For example, in week 3, the warm SST bias in the western Pacific induces warm surface temperature over the eastern CONUS, whereas a cold surface temperature bias dominates the whole CONUS in week 4 (see Fig. 10 in Stan et al. 2023). This time-varying bias pattern is insufficient to understand the source of errors in the model. In the case of precipitation, the tropical SST bias can explain up to 10% of the precipitation biases over the CONUS (Bai et al. 2023).

The objective of this study is to examine the bias in the surface air temperature over the CONUS during the boreal summer of 2011–17 in the UFS prototype 8 as well as identify the source of biases. The focus is on boreal summer to avoid the larger impacts of the Arctic and stratosphere that manifest in winter. To exclude the initialization effects, only the forecast bias from weeks 2 to 5 is considered. The large-scale spatial pattern of the weekly surface temperature bias is identified using the empirical orthogonal function (EOF; Wilks 2011) analysis. These biases are then related to the upper-level atmospheric teleconnection biases using both statistical and dynamical methods. The EOF analysis provides the largest variability of bias pattern rather than mean bias obtained by averaging forecast errors. The spread of bias in each forecast makes it more complicated to understand the behavior of the model and to correct than mean bias.

The description of UFS prototype 8, observational data, and used methodology are introduced in section 2. In section 3, the weekly bias and the most dominant bias pattern with related atmospheric fields are shown. The shortcomings of UFS prototype 8, with some possible reasons for the identified biases, are discussed in section 4. The summary and conclusions are given in section 5.

2. Model, data, and methods

a. Model

The UFS prototype 8 (UFS P8) is a fully coupled global model. The atmospheric component uses the Geophysical Fluid Dynamics Laboratory (GFDL) finite-volume cubed-sphere dynamical core, which has c384 (~0.25°) horizontal resolution and 127 vertical levels. The atmospheric physics package is the candidate for the Global Forecast System version 17 (GFSv17). The ocean model is GFDL Modular Ocean Model 6 (MOM6; Adcroft et al. 2019). The spatial resolution of MOM6 is a 0.25° tripolar grid with 75 hybrid vertical levels. The Los Alamos Sea Ice Model, version 6 (CICE6), WAVEWATCH III, and Goddard Chemistry Aerosol Radiation and Transport model (GOCART; Chin et al. 2000) are used for sea ice, waves, and aerosol components, respectively.

The reforecasts of UFS P8 are initialized on the first and 15th of each month from April 2011 to March 2018. The atmospheric initial conditions come from the Global Ensemble Forecast System, version 12 (GEFSv12), analysis (Hamill et al. 2022) and the initial conditions of waves are forced by GEFS. The land is initialized by the Noah-MP land model with a combination of Global Soil Wetness Project and GDAS atmospheric forcing, while snow is initialized from Noah-MP with NASA-GLDAS forcing. The ocean and sea ice are initialized by the CPC-3DVAR ocean data assimilation product (Adcroft et al. 2019) and CPC Sea Ice Initialization System (CPC-CSIS; Stefanova et al. 2022), respectively. Each reforecast extends to 35 days. In UFS P8, there is only a deterministic run for each initialization.

The stationary wave model (SWM) of Ting and Yu (1998) is used to understand the physical mechanisms driving the upper-level teleconnections. This is a dry dynamical core baroclinic model which can show a circulation response to diabatic heating forcing. The resolution of this model is the rhomboidal 30 (R30) truncation (2.25° latitude × 3.75° longitude) with 14 sigma vertical levels.

b. Data

The European Centre for Medium-Range Weather Forecasts (ECMWF) ERA5 reanalysis (Hersbach et al. 2020) is used as atmosphere observational data. The horizontal resolution of ERA5 is 0.25° in the latitude–longitude grid. Sea surface temperature is compared with the NOAA Optimal Interpolated SST, version 2 (OISSTv2; Reynolds et al. 2007), which has 0.25° horizontal resolution. The NOAA interpolation outgoing longwave radiation (OLR; Liebmann and Smith 1996) dataset is used for the analysis. Because NOAA OLR has a coarser resolution of 2.5° in latitude and longitude, the OLR from UFS P8 is regridded to 2.5°.

c. Methods

This study focuses on the lead 2–5 weeks of reforecasting during the extended boreal summer, June–September 2011–17. All UFS and ERA5 datasets are averaged in weekly means, and weekly biases are calculated as the difference between the weekly mean of UFS and ERA5 reanalysis (UFS P8–ERA5):

$$\text{weekly bias} = F_i - O_i, \tag{1}$$

where F_i and O_i are the weekly average of UFS P8 reforecast and ERA5 reanalysis, respectively. When the difference is calculated between anomalies, the time-varying difference is referred to as a forecasting error. Model anomalies do not include the systematic errors. The mean bias is then defined as the average of all weekly biases:

$$\text{mean bias} = \frac{\sum_i^N (F_i - O_i)}{N}, \tag{2}$$

where N is the total weekly forecasting cases from 2 to 5 weeks ($N = 224$).

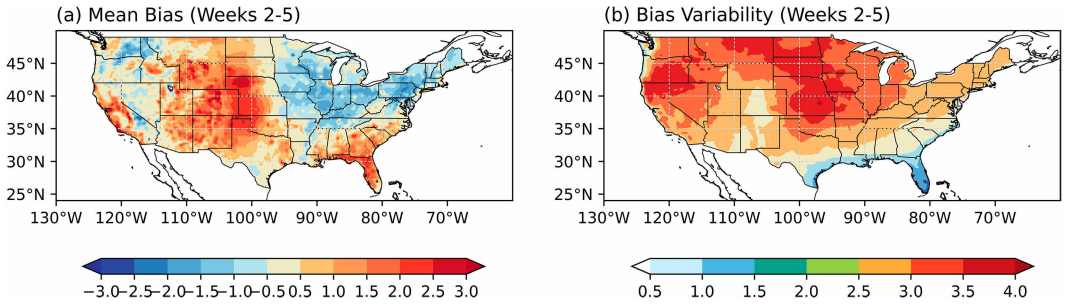

FIG. 1. Warm season (June–September). (a) Mean bias and (b) standard deviation of bias (°C) in UFS P8 surface air temperature compared to ERA5 during weeks 2–5 over the CONUS.

The variability of bias is calculated as the standard deviation of weekly biases.

The EOF analysis is applied to all weekly surface air temperature biases (224 samples: 7 years × 4 months × 2 initial dates × 4 weeks) over the CONUS (24°–50°N, 60°–130°W). The leading EOF represents the dominant pattern of the weekly bias, and the associated principal component (PC) shows the amplitude of bias in each of the 224 forecast samples. Linear regression of various variables on the PC is conducted to find sources of weekly bias (bias hereafter).

The ray-tracing algorithm introduced by Yang and Hoskins (1996) shows the trajectories of Rossby waves, which are derived from the dispersion relationship for Rossby waves:

$$\nu = \overline{u}k - \frac{\beta^* k}{(k^2 + l^2)^2}, \tag{3}$$

$$\beta^* = \frac{df}{dy} - \frac{\partial^2 \overline{U}}{\partial y^2}, \tag{4}$$

where ν is the wave frequency, $\overline{u}$ is the mean zonal wind, k and l are the zonal and meridional wavenumbers, respectively, and β^* is the meridional vorticity gradient with f as the Coriolis parameter. Then, the components of zonal and meridional group velocity of the Rossby wave are

$$C_{gx} = \frac{\partial \nu}{\partial k} = \overline{u} - \beta^* \frac{(k^2 - l^2)}{(k^2 + l^2)^2}, \tag{5}$$

$$C_{gy} = \frac{\partial \nu}{\partial l} = \beta^* \frac{2kl}{(k^2 + l^2)^2}. \tag{6}$$

Assuming stationary Rossby wave as $\nu = 0$, the trajectories are obtained from group velocity:

$$\frac{dx}{dt} = C_{gx} = \frac{2\overline{u}k^2}{(k^2 + l^2)}, \tag{7}$$

$$\frac{dy}{dt} = C_{gy} = \frac{2\overline{u}kl}{(k^2 + l^2)}. \tag{8}$$

In this study, the path of the Rossby wave is calculated following the methods of Rehbein et al. (2020), except for minor modification of zonally varying zonal wind at 500 hPa and turning latitude to trap the Rossby wave in midlatitudes. They used zonally averaged zonal wind and allowed the turning of the waves only once when $l^2 < 0$. These conditions produce waves with the same shape of trajectory at all longitudes (e.g., see Fig. 9 in Coelho et al. 2016). In this study, the zonal-mean zonal wind is replaced by the zonal wind, and turning is allowed for all waves when $l^2 < 0$ so that any wave can propagate along the waveguide (e.g., subtropical jet). Wavenumbers 1–9 are integrated for up to 30 days with 6 h of time step from every 5° grid point over 170°–185°E and 20°–35°N. The averaged wave paths are calculated as the average of longitude and latitude at the same time step when the wave propagates over 200°E.

The wave activity flux (WAF) defined by Takaya and Nakamura (2001) is a useful diagnostic for the propagation of the stationary Rossby wave and its components are defined as

$$F_x = \frac{p\cos\phi}{2|\mathbf{U}|}\left\{\frac{U}{a^2\cos^2\phi}\left[\left(\frac{\partial\psi'}{\partial\lambda}\right)^2 - \psi'\frac{\partial^2\psi'}{\partial\lambda^2}\right] + \frac{V}{a^2\cos^2\phi}\left(\frac{\partial\psi'}{\partial\lambda}\frac{\partial\psi'}{\partial\phi} - \psi'\frac{\partial^2\psi'}{\partial\lambda\partial\phi}\right)\right\}, \tag{9}$$

$$F_y = \frac{p\cos\phi}{2|\mathbf{U}|}\left\{\frac{U}{a^2\cos^2\phi}\left(\frac{\partial\psi'}{\partial\lambda}\frac{\partial\psi'}{\partial\phi} - \psi'\frac{\partial^2\psi'}{\partial\lambda\partial\phi}\right) + \frac{V}{a^2}\left[\left(\frac{\partial\psi'}{\partial\phi}\right)^2 - \psi'\frac{\partial^2\psi'}{\partial\phi^2}\right]\right\}, \tag{10}$$

where F_x and F_y are the zonal and meridional components of WAF at 500 hPa, respectively; a is the radius of Earth; p is the pressure; ϕ and λ are the latitude and longitude, respectively; $\mathbf{U}$ is 500-hPa wind vector which consists of zonal (U) and meridional (V) wind; and ψ' is a perturbation of streamfunction at 500 hPa. This perturbation is obtained by regression onto PC.

3. Surface air temperature bias pattern

Previous prototypes of UFS tend to have dipole surface air temperature bias patterns with warmer (colder) than observed over the western (eastern) CONUS (Stan et al. 2022). UFS P8 also shows a similar mean bias pattern in surface air temperature (Fig. 1a). During weeks 2–5, the largest warm mean bias is located over the Great Plains, presumably one of the most sensitive regions to land–atmosphere interactions

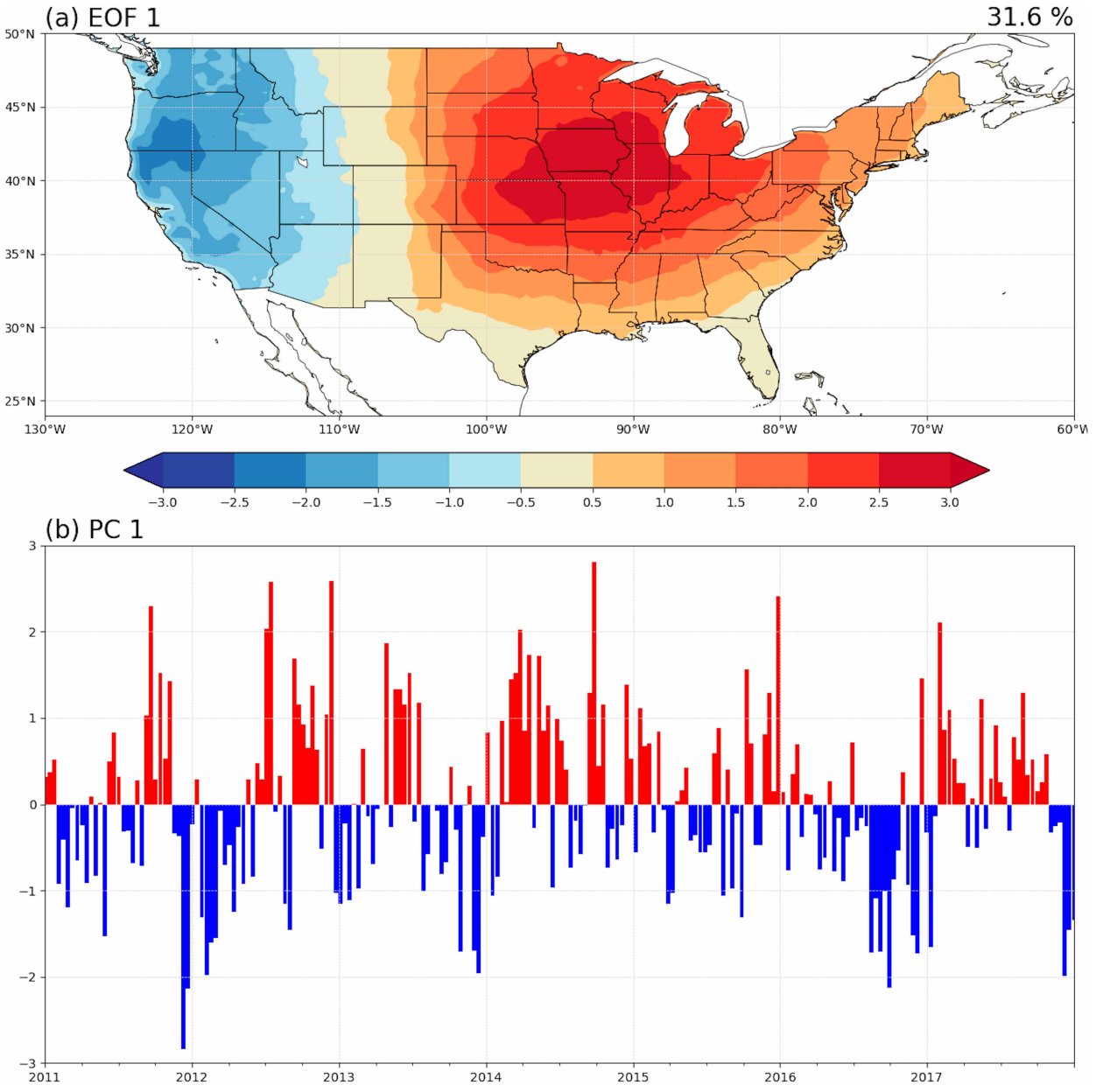

FIG. 2. (a) First EOF pattern (°C) of weekly surface air temperature bias over the CONUS and (b) related PC (unitless).

(Klein et al. 2006; Zhang et al. 2018). A cold bias dominates in the northeastern region of CONUS. These bias patterns are consistently shown in each week (Fig. S1 in the online supplemental material). According to Stan et al. (2022), this dipole bias pattern can be related to the SST bias over the tropical Pacific. The variability of temperature bias, measured by the standard deviation, tends to be larger than the amplitude of mean bias (Fig. 1b). For example, the variability of temperature bias over the western coast is 3 times larger than the mean bias. Unlike the mean bias, the two local maxima in variability are over the western coast and central CONUS. This result suggests that regions with the largest biases are not necessarily the regions with the most forecasting errors. The dominant pattern of mean bias can be determined through the EOF analysis described in section 2c applied to weeks 2–5.

Figure 2 shows the dominant EOF and related PC from surface air temperature bias over the CONUS. The EOF consists of a large-scale dipole pattern that explains 31.6% of the total bias variability and is consistent with the variability pattern seen in Fig. 1b. When the same analysis is conducted in each week (1–5), the spatial pattern of the dominant EOF is consistent with the results based on weeks 2–5 (supplemental Fig. 2) except for week 1 when initialization errors dominate. Therefore, all analyses are shown for the combined weeks 2–5.

TABLE 1. The correlation coefficient of PCs in each week. PCs are obtained from independent EOF analysis each week. Parenthesis indicates correlations of PCs from combined weeks (Fig. 2b).

Week	2	3	4	5
1	−0.23	−0.01	0.30	0.05
2		0.53 (0.49)	−0.18 (−0.16)	0.24 (0.25)
3			0.13 (0.15)	0.31 (0.30)
4				0.43 (0.42)

The PC indicates the amplitude and the sign of bias for each initialization date and week. Note that PCs of small amplitude do not indicate a lack of bias in the forecast. In the EOF analysis, the average of weekly biases is removed to construct an anomaly. Assuming the large contribution of biases comes from EOF1, the bias pattern is almost the same as the mean bias when the PC is 0. Time-varying bias seems almost independent of each week, even if they have the same initialization. Table 1 shows the lag correlation between each week. Although PC1 in week 2 has a correlation of 0.53 with week 3, the correlation between weeks 3 and 4 is only 0.13; some high correlation coefficients might be spurious correlations.

Next, to identify the potential drivers of the large-scale surface air temperature bias, Z500, SST, and OLR biases are regressed onto the PC1.

Figure 3 shows the regression patterns of Z500, SST, and OLR biases related to the surface air temperature bias over CONUS. In the upper-level atmosphere (Fig. 3a), there is a clear Rossby wave pattern from the Pacific to the Atlantic, which has a strong relationship with the dipole pattern of temperature bias over the CONUS. In the midlatitudes, the westerly background flow favors the Rossby wave to propagate eastward. In the case of SST (Fig. 3b), there are no significant signals over the tropics, indicating that surface air temperature bias over CONUS has a small relationship with tropical SST bias. Some zonal wave patterns are seen in the midlatitudes, which seem to be a response to the upper-level Rossby wave. The regression of OLR bias (Fig. 3c) suggests that convection in the tropical Pacific may be one of the dominant sources of temperature bias, instead of surface heating. There is significant convection over the tropical Pacific (purple box in Fig. 3c) that produces a wave train propagating to the CONUS, having consistency with 500-hPa geopotential height (Fig. 4a).

This relationship between the OLR bias over the tropical Pacific and temperature bias over the CONUS (Fig. 4b) also shows consistency with the surface air temperature bias pattern (Fig. 2a). Figure 4b indicates that OLR bias over the tropical Pacific is strongly related to temperature bias over the CONUS. The convection in the tropics is very challenging to forecast due to limitations in the parameterization of moist convective processes in the model. Figure 5 shows the mean bias of OLR and the anomaly correlation between the predicted OLR and NOAA OLR as a measure of UFS ability to predict tropical convection in the central Pacific during boreal summer. The anomaly correlation drops below 0.5 within 2 weeks. Thus, the improvement of OLR over the tropical Pacific has the potential to reduce temperature bias over the CONUS.

4. Background flow bias in UFS P8

The teleconnection between the tropics and midlatitudes on the subseasonal time scale provides an important source of predictability of the upper-level atmospheric circulation and weather over the CONUS (Stan et al. 2017). Consistent with the previous findings (e.g., Stan et al. 2023; Bai et al. 2023), the results of this study also emphasize the role of tropical Pacific forcing onto the extratropics (Fig. 3). However, almost all models have challenges in predicting teleconnections forced by the tropics (Vitart 2017; Stan et al. 2022). For example, the ECMWF model can predict the MJO over a month but the forecast skill for MJO teleconnection is much shorter (Vitart and Molteni 2010). This mismatch between the forecast skill of MJO itself and MJO teleconnections can be attributed to biases in upper-level circulation, as shown in Fig. 3b. Figure 6 shows regression patterns of ERA5 reanalysis and UFS P8 onto the corresponding OLR anomaly over the tropical central Pacific. In ERA5, the variability of OLR is associated with clear teleconnections across the CONUS (Fig. 6a) with a dipole temperature pattern (Fig. 6b). These patterns are very similar to the regression patterns on OLR bias (Fig. 4), which indicates the temperature variability over the CONUS is strongly related to convection over the tropical Pacific. In the case of UFS P8, the propagation of the Rossby wave is much weaker than in ERA5, showing a weak teleconnection and temperature response over the CONUS (Figs. 6c,d). Thus, even if the UFS P8 can provide perfect OLR variability over the tropical Pacific, the model has a bias over the CONUS due to the distorted link between the tropics and midlatitudes caused by the misrepresentation of teleconnections.

In the midlatitudes, the subtropical jet acts as a waveguide for the Rossby wave propagating eastward (Schubert et al. 2011), and especially in boreal summer, the Rossby wave can propagate circumglobally [e.g., circumglobal teleconnection (CGT); Ding and Wang 2005]. Thus, biases in midlatitudes mean flow, such as zonal wind and vertical wind shear, can influence the generation and propagation of the Rossby wave in the model. Figure 7 shows the bias of 500-hPa zonal wind and vertical wind shear calculated as the difference between 200- and 850-hPa zonal wind. In the midlatitude Pacific, the UFS P8 has weaker zonal wind at 500 hPa and stronger vertical shear than in reanalysis. First, a bias in the zonal wind can produce a weak waveguide in UFS P8, which cannot trap the zonally propagating waves. The WAF in ERA5 shows a clear propagation of waves starting from the central tropical Pacific to the North Atlantic, while in UFS, the Rossby wave propagation is deflected southward over the northeastern Pacific (Fig. 7a). According to Fandry and Leslie (1984), an idealized Rossby wave has a lower frequency and weaker amplitude when the vertical wind shear is strong. In UFS P8, the wavelength and amplitude of the wave are slightly longer and smaller than in ERA5, respectively (Fig. 7b).

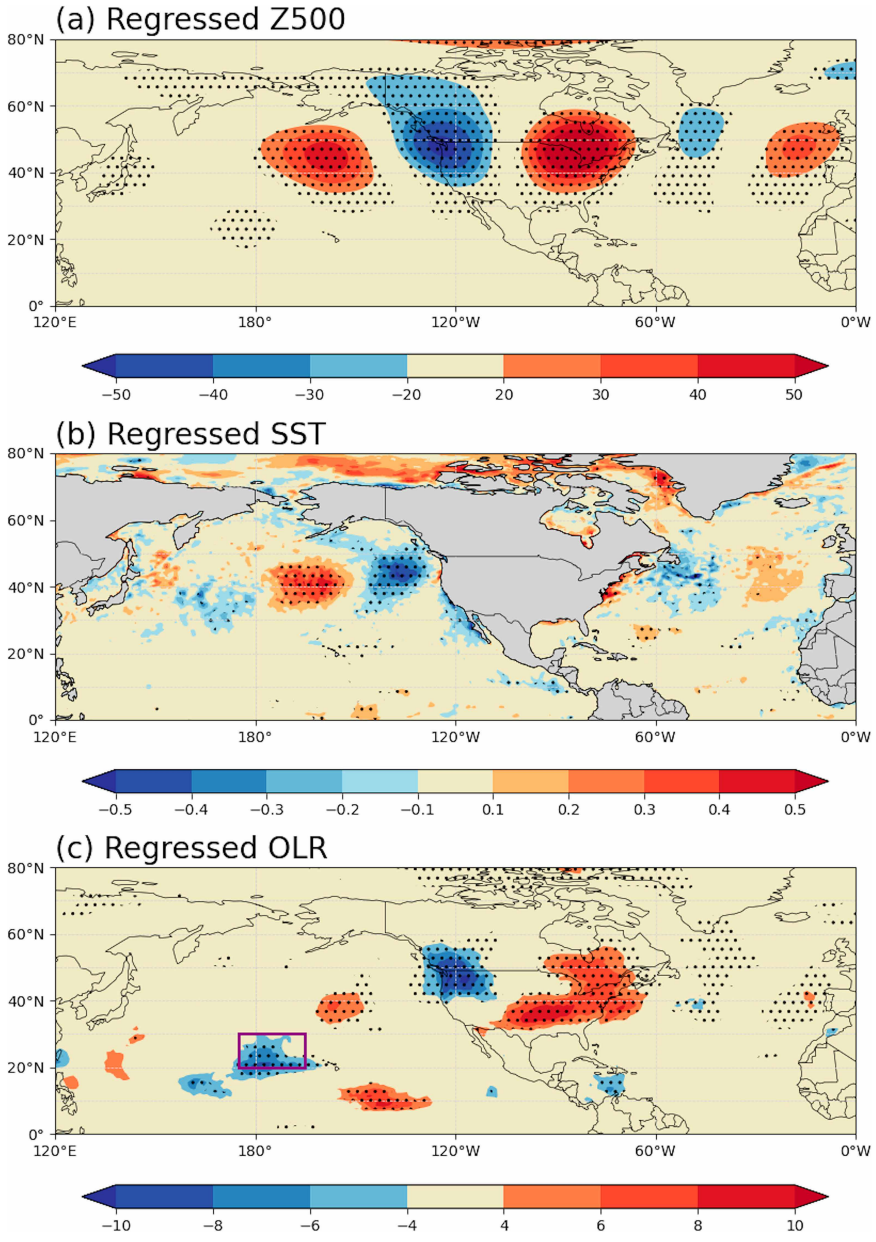

FIG. 3. The regressed bias of (a) 500-hPa geopotential height (m), (b) sea surface temperature (°C), and (c) OLR (W m^{-2}) on PC1. The dotted area indicates statistically significant at 0.01.

These differences in the propagation of the Rossby wave are more clearly shown using the ray tracing methodology. Figure 8 shows the trajectories of Rossby waves from wavenumbers 1 to 9, which are grouped as wavenumber 1–2, 3–6, and 7–9. The longwave (wavenumbers 1–2) Rossby waves tend to have a northward path, and the shortwave (wavenumbers 7–9) Rossby waves propagate on a southward path. When the zonal wavenumber is between 3 and 6, the Rossby wave path is well matched with the upper-level circulations (Fig. 8a) and propagates eastward in the midlatitudes band, which is the waveguide effect. The waves with wavenumbers 7–9 propagate eastward parallel to the equator. In UFS P8, some wave paths pass over the CONUS, but most of the wave paths are undefined or sunk off the West Coast of the CONUS. For wavenumbers 3–6, this wave path matches the upper-level circulations only over the western CONUS (Figs. 6c and 8b). In addition, in the model, the weaker center of action located in northeastern Canada can be explained by the inability of longer waves (wavenumbers 1–2) to reach this region and stronger vertical wind shear than in ERA5.

To further explore the role of OLR and mean state biases, an idealized model experiment is conducted to examine the upper-tropospheric teleconnection generated by OLR variability using the SWM. In the experiment, the diabatic heating

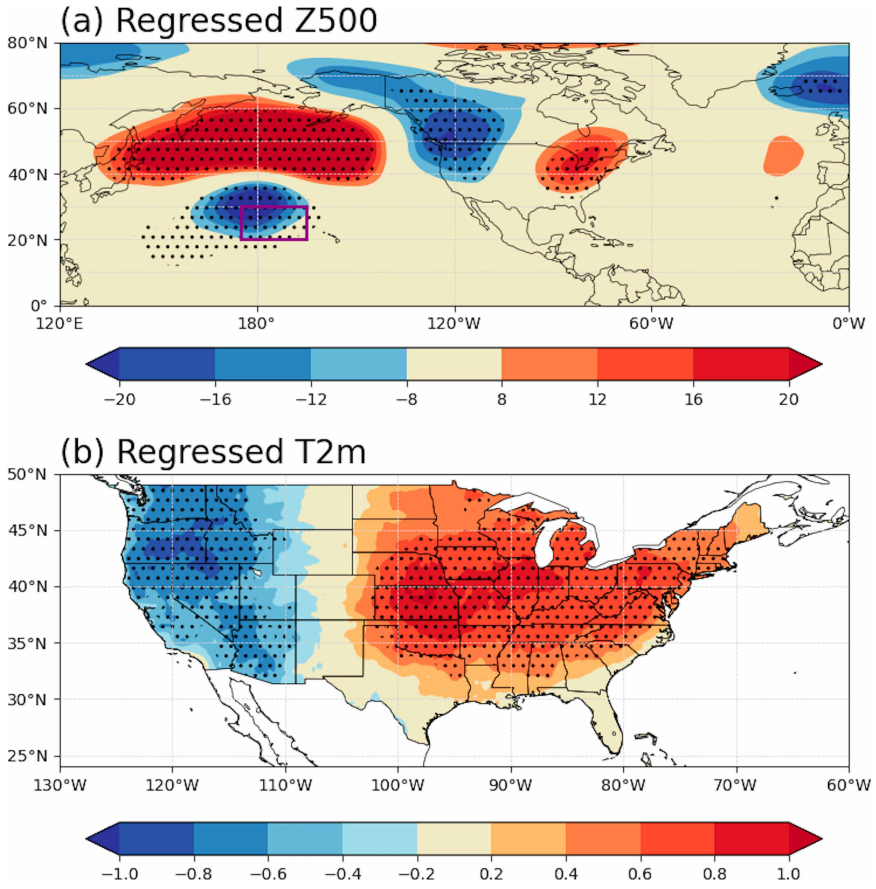

FIG. 4. The regressed bias of (a) 500-hPa geopotential height (m) and (b) surface air temperature (°C) on averaged OLR bias over the central Pacific (20°–30°N, 175°E–165°W). The dotted area indicates statistically significant at 0.01. For consistency, the sign of OLR bias is flipped.

forcing is located in the central Pacific (20°–30°N, 175°E–165°W), mimicking the negative OLR anomaly. The forcing is maximum at 0.5682 sigma level, following an idealized diabatic heating profile of deep convection (e.g., Schumacher et al. 2007). The background fields, including wind, temperature, and surface pressure, are prescribed from ERA5 and averaged between 2011 and 2017 June–September (JJAS). The simulation is integrated for 30 days. Figure 9 shows the response of streamfunction to the diabatic heating forcing. The response consists of upper-level circulations over the North Pacific, showing the Rossby wave train from the central Pacific to the Atlantic. Each node of the wave matches the regression pattern in ERA5 (Fig. 6a). The unrealistic response in the tropics is likely caused by the idealized settings of the model.

The experiments are then repeated using all background fields from UFS P8 (Fig. 9a) and a combination of one field from UFS P8 (e.g., temperature: Fig. 9b; zonal wind: Fig. 9c; meridional wind: Fig. 9d) and the others from ERA5. In the experiment with the background zonal winds from UFS P8, the upper-level wave pattern is shifted westward as shown in Figs. 7b and 8b. The experiments using temperature (Fig. 9b) and meridional wind (Fig. 9d) show that these two fields have

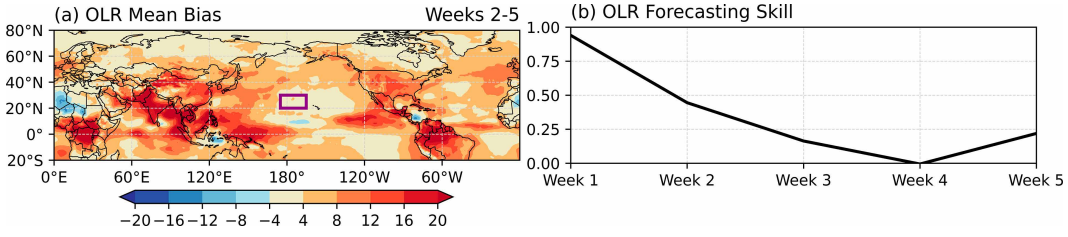

FIG. 5. (a) Spatial distribution of mean bias of OLR (W m^{-2}) during weeks 2–5 and (b) anomaly correlation of OLR in UFS P8 over the central Pacific [20°–30°N, 175°E–165°W, purple box in (a)].

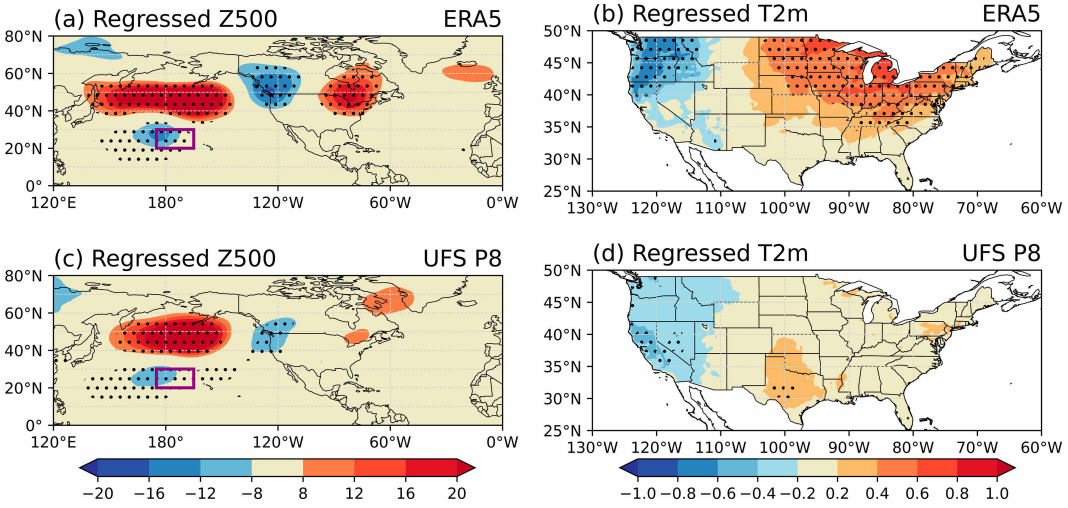

FIG. 6. Regression coefficient of (left) 500-hPa geopotential height (m) and (right) surface air temperature anomaly (°C) in (top) ERA5 reanalysis and (bottom) UFS P8 on averaged OLR anomaly over the central Pacific (20°–30°N, 175°E–165°W, purple box), respectively. The dotted area indicates statistically significant at 0.01. For convenience, signs are flipped.

smaller impacts on the midlatitudes, demonstrating that biases in the zonal wind including vertical wind shear can explain the degradation of the upper-level Rossby wave seen in UFS P8.

In summary, the bias of background flow seems to contribute to the bias in representing the tropics to midlatitudes teleconnections on the S2S time scale. In UFS P8, the weak zonal wind slows down the eastward propagation of the Rossby

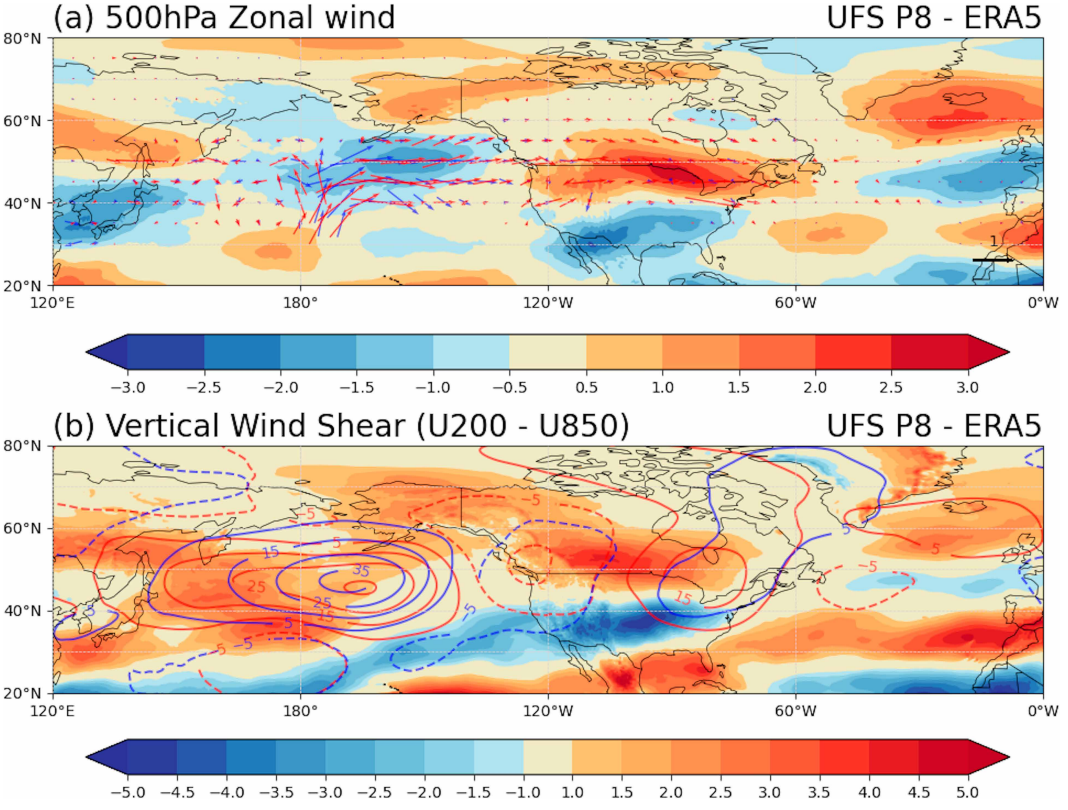

FIG. 7. Difference of (a) 500-hPa zonal wind (m s^{-1}) and (b) vertical wind shear (200–850-hPa zonal wind, m s^{-1}) between ERA5 and UFS P8 with the regressed WAF (vector, m^2 s^{-2}) and 500-hPa geopotential height (m) on the central Pacific OLR in ERA5 (red) and UFS P8 (blue), respectively.

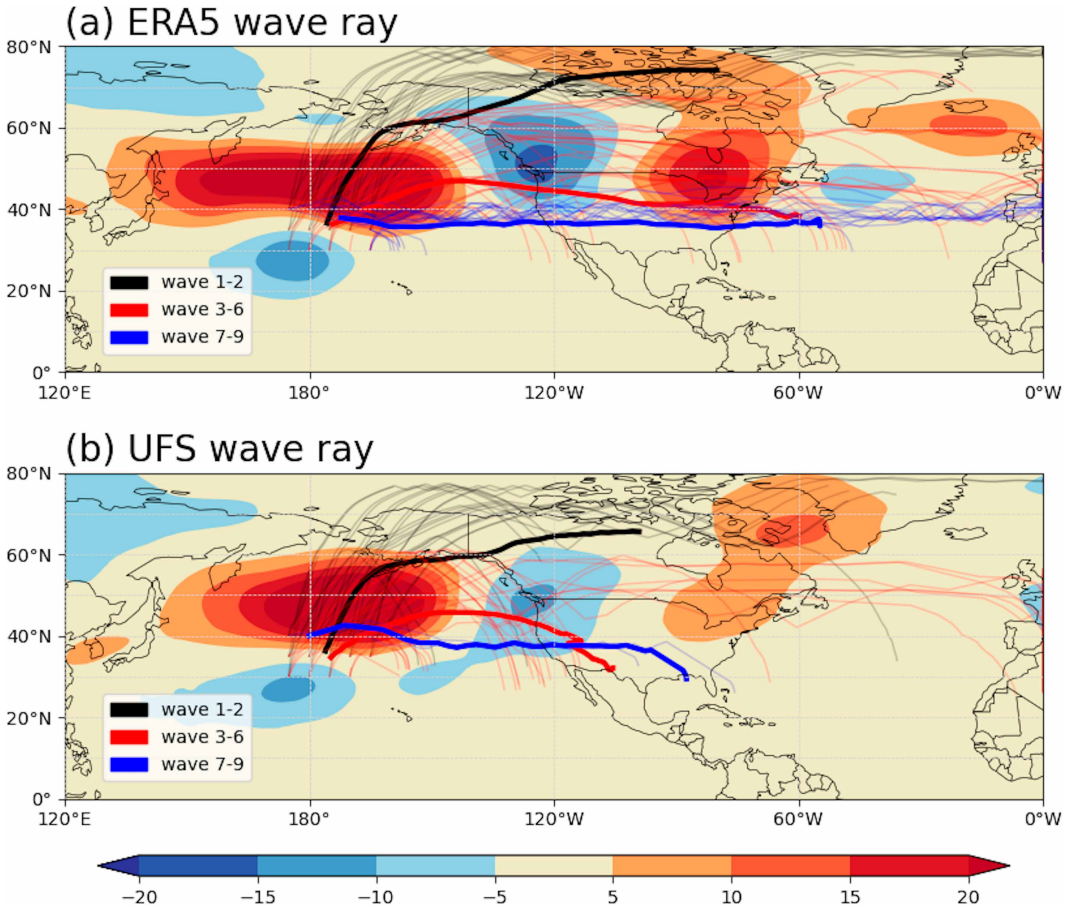

FIG. 8. Ray tracing of wavenumbers 1–2 (black), wavenumbers 3–6 (red), and wavenumbers 7–9 (blue) in (a) ERA5 and (b) UFS P8. The solid line indicates the averaged path of each group of wavenumbers when the wave propagates east of 200°E. Shaded is as in Figs. 6a and 6c.

waves, which, along with strong vertical wind shear, are not favorable conditions for stationary waves with longer wavelengths and weak amplitude.

5. Summary and conclusions

This study aims to identify and analyze potential factors contributing to the variability of surface air temperature bias across the CONUS within the UFS P8 model. The mean bias of UFS P8 is similar to the bias identified in previous prototypes as shown by Stan et al. (2022) and Bai et al. (2023). Using an EOF analysis, the structure of the largest variability of the surface air temperature bias emerges as an east–west dipole pattern over the CONUS. This methodology diagnoses the spatial structure of bias and defines a bias index associated with the bias pattern. The large-scale bias pattern in UFS P8 explains 31.6% of total bias variability and is strongly related to upper-level atmospheric circulation originating from the tropical central Pacific. The results suggest that the OLR bias over the tropical central Pacific generates a wave-like bias pattern in the upper atmosphere and affects the surface air temperature in the extratropics. A similar wave-like bias pattern was identified in previous UFS prototypes, but the source of bias was associated with the tropical SST bias (Stan et al. 2023; Bai et al. 2023).

Representing teleconnection from the tropics to midlatitudes is one of the challenges of the S2S forecasting models (Stan et al. 2022). UFS P8 also shows weak propagation of the Rossby wave from the tropical central Pacific to the CONUS, indicating even if the model produces perfect convective activity in the tropics, there can be biases in the midlatitudes affecting the propagation of the Rossby wave. In ERA5, convection over the tropics can excite Rossby waves that propagate eastward across North America and modulate the surface air temperature over the CONUS. In UFS P8, the response of the surface air temperature to tropical convection predicted by the model results in a weaker signal over the CONUS than the response seen in ERA5. UFS P8 has weak zonal winds at 500 hPa over the North Pacific, where the Rossby wave path is typically located in ERA5. This bias prevents the propagation of waves with wavenumbers from 1 through 9 in the model. In addition, UFS P8 has stronger vertical wind shear, which can generate longer wavelengths and weaken the amplitude of stationary Rossby waves. These

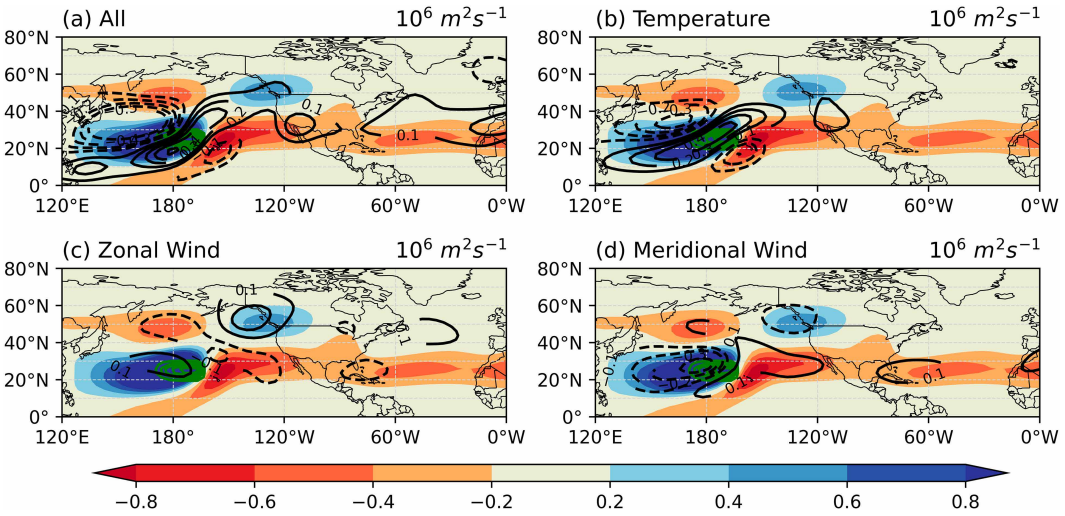

FIG. 9. Streamfunction response (shaded in all figures, 10^6 m^2 s^{-1}) to diabatic heating (green contour) in the SWM model with ERA5 background fields (2011–17 JJAS). The diabatic heating represents negative OLR anomaly (active convection). The black contours indicate the difference in response when using (a) all background fields, (b) temperature, (c) zonal wind, and (d) meridional wind from UFS P8.

biases of background flow in UFS P8 can degrade the model's ability to represent teleconnections from the tropics.

The bias in zonal mean flow predicted by UFS P8 can come from multiple sources. First, deficiencies in the sea ice model. Barton et al. (2023) reported that UFS P8 has a strong negative bias in Arctic sea ice extent, especially stronger in summer due to a negative bias in the sea ice initial conditions. The negative bias of sea ice can drive a warm Arctic with a reduced meridional temperature gradient in midlatitudes, which can reduce subtropical jets, as shown in the weak zonal wind in UFS P8. Second, the ocean model used in UFS P8 has a typical warm SST bias in the North Pacific near the Bering Sea (supplemental Fig. 3). Sun et al. (2018) and Bai et al. (2023) reported a similar strong warm bias in the North Pacific in CFS, version 2 (CFSv2), and UFS prototype 6, respectively. Although CFSv2 uses MOM version 4 for ocean components, these models all use MOM as an ocean component, suggesting warm SST in the North Pacific might come from the common errors in the MOM ocean model. The warm SST can reduce the strength of the subtropical jet. These biases can significantly reduce the meridional temperature gradient and further weaken the zonal wind (supplemental Fig. 4). Model

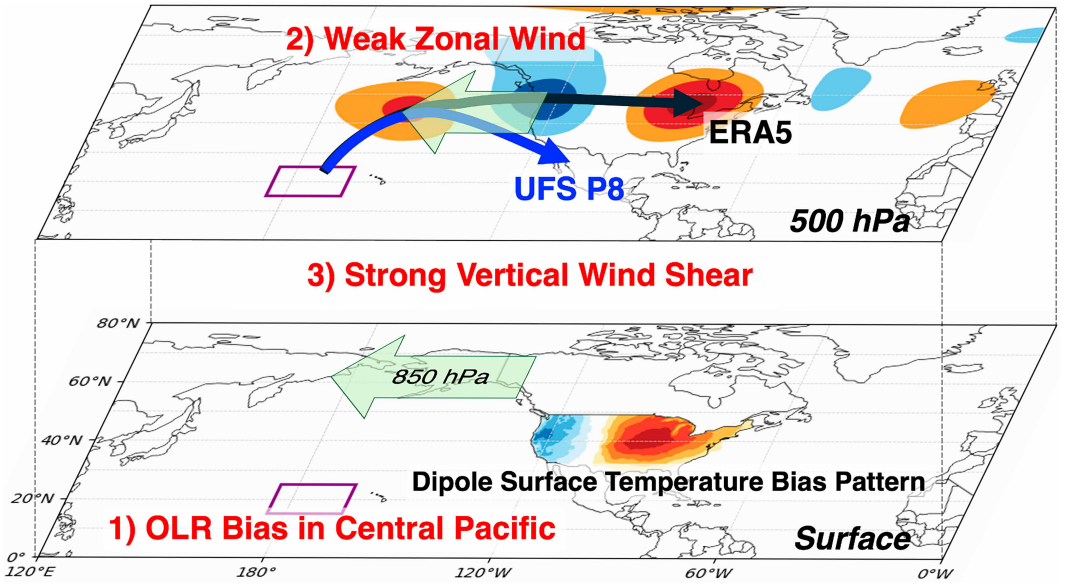

FIG. 10. The schematic diagram for three error sources of surface air temperature bias pattern in UFS P8. Thick arrows indicate teleconnection paths in ERA5 (black) and UFS P8 (blue), respectively.

development to reduce these biases can also improve the representation of upper-level teleconnection and forecasting of surface air temperature over the CONUS in UFS P8. Furthermore, Slingo and Slingo (1988) suggested that the longwave cloud radiative effects can affect the strength of subtropical jets. Because UFS P8 does not have the variables for clear sky longwave radiation, biases in longwave cloud radiation effects cannot be evaluated.

The source of biases affecting the boreal summer surface air temperature biases over the CONUS is summarized in the schematic shown in Fig. 10. The surface air temperature bias is strongly related to the upper-level Rossby wave from the tropics. 1) This Rossby wave appears as excited by the OLR bias in the central tropical Pacific. In addition, even if convection in the tropics is well represented, 2) the weak zonal wind at 500 hPa or upper-level atmosphere reduces eastward propagation of the Rossby wave, and 3) the strong vertical wind shear bias can suppress the amplitude of the Rossby wave.

Acknowledgments. This study was supported by the Unified Forecast System Research to Operation (UFS R2O) Project which is jointly funded by NOAA's Office of Science and Technology Integration (OSTI) of National Weather Service (NWS) and Weather Program Office (WPO) [Joint Technology Transfer Initiative (JTTI)] of the Office of Oceanic and Atmospheric Research (OAR) through the NOAA Grant NA19NES4320002 [Cooperative Institute for Satellite Earth System Studies (CISESS)]. We appreciate Rehbein et al. (2020) for the public release of the R script of the Rossby wave (https://github.com/salvatirehbein/raytracing). Computational support for analysis was provided by the Office of Research Computing at George Mason University.

Data availability statement. UFS prototype 8 hindcast data are available at https://registry.opendata.aws/noaa-ufs-s2s/. ERA5 reanalysis was downloaded from the Copernicus Climate Change Service at https://climate.copernicus.eu/climate-reanalysis. NOAA OISSTv2 high-resolution dataset and interpolated outgoing longwave radiation (OLR) data provided by the NOAA PSL, Boulder, Colorado, USA, from their website at https://psl.noaa.gov.

REFERENCES

Adcroft, A., and Coauthors, 2019: The GFDL global ocean and sea ice model OM4.0: Model description and simulation features. *J. Adv. Model. Earth Syst.*, **11**, 3167–3211, https://doi.org/10.1029/2019MS001726.

Bai, H., and Coauthors, 2023: The impact of tropical SST biases on the S2S precipitation forecast skill over the contiguous United States in the UFS global coupled model. *Wea. Forecasting*, **38**, 937–952, https://doi.org/10.1175/WAF-D-22-0162.1.

Barton, N., R. Grumbine, D. Dukhovskoy, P. Pegion, and A. Mehra, 2023: Diagnosing Sea Ice in the Unified Forecast System (UFS). Environmental Modeling Center (EMC)/National Oceanic and Atmospheric Administration (NOAA), 21 pp., https://epic.noaa.gov/wp-content/uploads/2023/08/UIFCW-2023-Fri-3.-Barton_Neil_Diagnosing-Sea-Ice-in-the-Unified-Forecast-System-UFS_.pdf.

Chin, M., R. B. Rood, S.-J. Lin, J.-F. Müller, and A. M. Thompson, 2000: Atmospheric sulfur cycle simulated in the global model GOCART: Model description and global properties. *J. Geophys. Res.*, **105**, 24 671–24 687, https://doi.org/10.1029/2000JD900384.

Coelho, C. A. S., and Coauthors, 2016: The 2014 southeast Brazil austral summer drought: Regional scale mechanisms and teleconnections. *Climate Dyn.*, **46**, 3737–3752, https://doi.org/10.1007/s00382-015-2800-1.

Delworth, T. L., and Coauthors, 2020: SPEAR: The next generation GFDL modeling system for seasonal to multidecadal prediction and projection. *J. Adv. Model. Earth Syst.*, **12**, e2019MS001895, https://doi.org/10.1029/2019MS001895.

Ding, Q., and B. Wang, 2005: Circumglobal teleconnection in the Northern Hemisphere summer. *J. Climate*, **18**, 3483–3505, https://doi.org/10.1175/JCLI3473.1.

Dirmeyer, P. A., P. Gentine, M. B. Ek, and G. Balsamo, 2019: Land surface processes relevant to sub-seasonal to seasonal (S2S) prediction. *Sub-Seasonal to Seasonal Prediction*, Elsevier, 165–181.

Domeisen, D. I. V., and Coauthors, 2020: The role of the stratosphere in subseasonal to seasonal prediction: 2. Predictability arising from stratosphere-troposphere coupling. *J. Geophys. Res. Atmos.*, **125**, e2019JD030923, https://doi.org/10.1029/2019JD030923.

——, and Coauthors, 2022: Advances in the subseasonal prediction of extreme events: Relevant case studies across the globe. *Bull. Amer. Meteor. Soc.*, **103**, E1473–E1501, https://doi.org/10.1175/BAMS-D-20-0221.1.

Fandry, C. B., and L. M. Leslie, 1984: The effects of vertical shear and stratification on stationary Rossby waves. *Geophys. Astrophys. Fluid Dyn.*, **29**, 305–332, https://doi.org/10.1080/03091928408248193.

Guemas, V., and Coauthors, 2016: A review on Arctic sea-ice predictability and prediction on seasonal to decadal timescales. *Quart. J. Roy. Meteor. Soc.*, **142**, 546–561, https://doi.org/10.1002/qj.2401.

Hamill, T. M., and Coauthors, 2022: The reanalysis for the Global Ensemble Forecast System, version 12. *Mon. Wea. Rev.*, **150**, 59–79, https://doi.org/10.1175/MWR-D-21-0023.1.

Hersbach, H., and Coauthors, 2020: The ERA5 global reanalysis. *Quart. J. Roy. Meteor. Soc.*, **146**, 1999–2049, https://doi.org/10.1002/qj.3803.

Jenney, A. M., K. M. Nardi, E. A. Barnes, and D. A. Randall, 2019: The seasonality and regionality of MJO impacts on North American temperature. *Geophys. Res. Lett.*, **46**, 9193–9202, https://doi.org/10.1029/2019GL083950.

Jong, B.-T., M. Ting, and R. Seager, 2021: Assessing ENSO summer teleconnections, impacts, and predictability in North America. *J. Climate*, **34**, 3629–3643, https://doi.org/10.1175/JCLI-D-20-0761.1.

Klein, S. A., X. Jiang, J. Boyle, S. Malyshev, and S. Xie, 2006: Diagnosis of the summertime warm and dry bias over the U.S. Southern Great Plains in the GFDL climate model using a weather forecasting approach. *Geophys. Res. Lett.*, **33**, L18805, https://doi.org/10.1029/2006GL027567.

Koster, R. D., and Coauthors, 2010: Contribution of land surface initialization to subseasonal forecast skill: First results from a multi-model experiment. *Geophys. Res. Lett.*, **37**, L02402, https://doi.org/10.1029/2009GL041677.

Krishnamurthy, V., and C. Stan, 2022: Prediction of extreme events in precipitation and temperature over CONUS during boreal summer in the UFS coupled model. *Climate Dyn.*, **59**, 109–125, https://doi.org/10.1007/s00382-021-06120-0.

——, and Coauthors, 2021: Sources of subseasonal predictability over CONUS during boreal summer. *J. Climate*, **34**, 3273–3294, https://doi.org/10.1175/JCLI-D-20-0586.1.

Liebmann, B., and C. Smith, 1996: Description of a complete (interpolated) outgoing longwave radiation dataset. *Bull. Amer. Meteor. Soc.*, **77**, 1275–1277, https://doi.org/10.1175/1520-0477-77.6.1274.

Lin, H., J. Frederiksen, D. Straus, and C. Stan, 2019: Tropical-extratropical interactions and teleconnections. *Sub-Seasonal to Seasonal Prediction*, Elsevier, 143–164.

Meehl, G. A., 1995: Global coupled general circulation models. *Bull. Amer. Meteor. Soc.*, **76**, 951–957, https://doi.org/10.1175/1520-0477-76.6.951.

Merz, B., and Coauthors, 2020: Impact forecasting to support emergency management of natural hazards. *Rev. Geophys.*, **58**, e2020RG000704, https://doi.org/10.1029/2020RG000704.

Molod, A., and Coauthors, 2020: GEOS-S2S version 2: The GMAO high-resolution coupled model and assimilation system for seasonal prediction. *J. Geophys. Res. Atmos.*, **125**, e2019JD031767, https://doi.org/10.1029/2019JD031767.

Orsolini, Y. J., R. Senan, G. Balsamo, F. J. Doblas-Reyes, F. Vitart, A. Weisheimer, A. Carrasco, and R. E. Benestad, 2013: Impact of snow initialization on sub-seasonal forecasts. *Climate Dyn.*, **41**, 1969–1982, https://doi.org/10.1007/s00382-013-1782-0.

Park, C.-H., J. Choi, S.-W. Son, D. Kim, S.-W. Yeh, and J.-S. Kug, 2023: Sub-seasonal variability of ENSO teleconnections in western North America and its prediction skill. *J. Geophys. Res. Atmos.*, **128**, e2022JD037985, https://doi.org/10.1029/2022JD037985.

Peng, P., and A. Kumar, 2005: A large ensemble analysis of the influence of tropical SSTs on seasonal atmospheric variability. *J. Climate*, **18**, 1068–1085, https://doi.org/10.1175/JCLI-3314.1.

Rehbein, A., T. Ambrizzi, S. Ibarra-Espinosa, and L. M. M. Dutra, 2020: Rossby wave ray tracing v0.1.0. Accessed 23 January 2024, https://github.com/salvatirehbein/raytracing.

Reynolds, R. W., T. M. Smith, C. Liu, D. B. Chelton, K. S. Casey, and M. G. Schlax, 2007: Daily high-resolution-blended analyses for sea surface temperature. *J. Climate*, **20**, 5473–5496, https://doi.org/10.1175/2007JCLI1824.1.

Robertson, A. W., A. Kumar, M. Peña, and F. Vitart, 2015: Improving and promoting subseasonal to seasonal prediction. *Bull. Amer. Meteor. Soc.*, **96**, ES49–ES53, https://doi.org/10.1175/BAMS-D-14-00139.1.

——, F. Vitart, and S. J. Camargo, 2020: Subseasonal to seasonal prediction of weather to climate with application to tropical cyclones. *J. Geophys. Res. Atmos.*, **125**, e2018JD029375, https://doi.org/10.1029/2018JD029375.

Saha, S., and Coauthors, 2006: The NCEP climate forecast system. *J. Climate*, **19**, 3483–3517, https://doi.org/10.1175/JCLI3812.1.

Saravanan, R., and P. Chang, 2019: Midlatitude mesoscale ocean-atmosphere interaction and its relevance to S2S prediction. *Sub-Seasonal to Seasonal Prediction*, Elsevier, 183–200.

Schubert, S., H. Wang, and M. Suarez, 2011: Warm season subseasonal variability and climate extremes in the Northern Hemisphere: The role of stationary Rossby waves. *J. Climate*, **24**, 4773–4792, https://doi.org/10.1175/JCLI-D-10-05035.1.

Schumacher, C., M. H. Zhang, and P. E. Ciesielski, 2007: Heating structures of the TRMM field campaigns. *J. Atmos. Sci.*, **64**, 2593–2610, https://doi.org/10.1175/JAS3938.1.

Seo, E., P. A. Dirmeyer, M. Barlage, H. Wei, and M. Ek, 2024: Evaluation of land–atmosphere coupling processes and climatological bias in the UFS global coupled model. *J. Hydrometeor.*, **25**, 161–175, https://doi.org/10.1175/JHM-D-23-0097.1.

Slingo, A., and J. M. Slingo, 1988: The response of a general circulation model to cloud longwave radiative forcing. I: Introduction and initial experiments. *Quart. J. Roy. Meteor. Soc.*, **114**, 1027–1062, https://doi.org/10.1002/qj.49711448209.

Stan, C., D. M. Straus, J. S. Frederiksen, H. Lin, E. D. Maloney, and C. Schumacher, 2017: Review of tropical-extratropical teleconnections on intraseasonal time scales. *Rev. Geophys.*, **55**, 902–937, https://doi.org/10.1002/2016RG000538.

——, and Coauthors, 2022: Advances in the prediction of MJO teleconnections in the S2S forecast systems. *Bull. Amer. Meteor. Soc.*, **103**, E1426–E1447, https://doi.org/10.1175/BAMS-D-21-0130.1.

——, and Coauthors, 2023: The impact of tropical Pacific SST biases on the S2S forecast skill over North America in the UFS global coupled model. *J. Climate*, **36**, 2439–2456, https://doi.org/10.1175/JCLI-D-22-0196.1.

Stefanova, L., and Coauthors, 2022: Description and results from UFS coupled prototypes for future global, ensemble and seasonal forecasts at NCEP. NCEP Office Note 510, 201 pp., https://doi.org/10.25923/knxm-kz26.

Sun, S., R. Bleck, S. G. Benjamin, B. W. Green, and G. A. Grell, 2018: Subseasonal forecasting with an icosahedral, vertically quasi-Lagrangian coupled model. Part I: Model overview and evaluation of systematic errors. *Mon. Wea. Rev.*, **146**, 1601–1617, https://doi.org/10.1175/MWR-D-18-0006.1.

Takaya, K., and H. Nakamura, 2001: A formulation of a phase-independent wave-activity flux for stationary and migratory quasigeostrophic eddies on a zonally varying basic flow. *J. Atmos. Sci.*, **58**, 608–627, https://doi.org/10.1175/1520-0469(2001)058<0608:AFOAPI>2.0.CO;2.

Ting, M., and L. Yu, 1998: Steady response to tropical heating in wavy linear and nonlinear baroclinic models. *J. Atmos. Sci.*, **55**, 3565–3582, https://doi.org/10.1175/1520-0469(1998)055<3565:SRTTHI>2.0.CO;2.

Vitart, F., 2014: Evolution of ECMWF sub-seasonal forecast skill scores. *Quart. J. Roy. Meteor. Soc.*, **140**, 1889–1899, https://doi.org/10.1002/qj.2256.

——, 2017: Madden—Julian oscillation prediction and teleconnections in the S2S database. *Quart. J. Roy. Meteor. Soc.*, **143**, 2210–2220, https://doi.org/10.1002/qj.3079.

——, and F. Molteni, 2010: Simulation of the Madden–Julian oscillation and its teleconnections in the ECMWF forecast system. *Quart. J. Roy. Meteor. Soc.*, **136**, 842–855, https://doi.org/10.1002/qj.623.

——, and A. W. Robertson, 2018: The sub-seasonal to seasonal prediction project (S2S) and the prediction of extreme events. *npj Climate Atmos. Sci.*, **1**, 3, https://doi.org/10.1038/s41612-018-0013-0.

——, and Coauthors, 2019: Sub-seasonal to seasonal prediction of weather extremes. *Sub-Seasonal to Seasonal Prediction*, Elsevier, 365–386.

White, C. J., and Coauthors, 2017: Potential applications of subseasonal-to-seasonal (S2S) predictions. *Meteor. Appl.*, **24**, 315–325, https://doi.org/10.1002/met.1654.

——, and Coauthors, 2022: Advances in the application and utility of subseasonal-to-seasonal predictions. *Bull. Amer. Meteor. Soc.*, **103**, E1448–E1472, https://doi.org/10.1175/BAMS-D-20-0224.1.

Wilks, D. S., 2011: Principal component (EOF) analysis. *Statistical Methods in the Atmospheric Sciences*, International Geophysics, Vol. 100, Academic Press, 519–562.

Williams, K. D., and Coauthors, 2018: The Met Office Global Coupled Model 3.0 and 3.1 (GC3.0 and GC3.1) configurations. *J. Adv. Model. Earth Syst.*, **10**, 357–380, https://doi.org/10.1002/2017MS001115.

Williams, N. C., A. A. Scaife, and J. A. Screen, 2023: Underpredicted ENSO teleconnections in seasonal forecasts. *Geophys. Res. Lett.*, **50**, e2022GL101689, https://doi.org/10.1029/2022GL101689.

Yang, G.-Y., and B. J. Hoskins, 1996: Propagation of Rossby waves of nonzero frequency. *J. Atmos. Sci.*, **53**, 2365–2378, https://doi.org/10.1175/1520-0469(1996)053<2365:PORWON>2.0.CO;2.

Zhang, C., S. Xie, S. A. Klein, H.-y. Ma, S. Tang, K. V. Weverberg, C. J. Morcrette, and J. Petch, 2018: CAUSES: Diagnosis of the summertime warm bias in CMIP5 climate models at the ARM Southern Great Plains site. *J. Geophys. Res. Atmos.*, **123**, 2968–2992, https://doi.org/10.1002/2017JD027200.